

Multi-fidelity data fusion through parameter space reduction with applications to automotive engineering

Francesco Romor^{*a}, Marco Tezzele^{†a}, Markus Mrosek^{‡b}, Carsten Othmer^{§b}, and
Gianluigi Rozza^{¶a}

^aMathematics Area, mathLab, SISSA, via Bonomea 265, I-34136 Trieste, Italy

^bVolkswagen AG, Innovation Center Europe, 38436 Wolfsburg, Germany

July 11, 2023

Abstract

Multi-fidelity models are of great importance due to their capability of fusing information coming from different numerical simulations, surrogates, and sensors. We focus on the approximation of high-dimensional scalar functions with low intrinsic dimensionality. By introducing a low dimensional bias we can fight the curse of dimensionality affecting these quantities of interest, especially for many-query applications. We seek a gradient-based reduction of the parameter space through linear active subspaces or a nonlinear transformation of the input space. Then we build a low-fidelity response surface based on such reduction, thus enabling nonlinear autoregressive multi-fidelity Gaussian process regression without the need of running new simulations with simplified physical models. This has a great potential in the data scarcity regime affecting many engineering applications. In this work we present a new multi-fidelity approach that involves active subspaces and the nonlinear level-set learning method, starting from the preliminary analysis previously conducted [45]. The proposed framework is tested on two high-dimensional benchmark functions, and on a more complex car aerodynamics problem. We show how a low intrinsic dimensionality bias can increase the accuracy of Gaussian process response surfaces.

1 Introduction

The curse of dimensionality affects the realization of reliable models for high-dimensional functions approximation. This problem is particularly evident in the data scarcity regime which characterizes many industrial and engineering applications. We address this issue by exploiting parameter space reduction techniques in a multi-fidelity setting.

Gaussian processes (GP) [54] have spread in many fields as a reliable regression (GPR) method, especially for optimization and inverse problems. Many extensions stemmed from the original formulation, such as for kernel methods [21], and for big data and memory limitations [26, 29]. On the other hand the exploitation of multi-fidelity models had a huge impact in the scientific computing community thanks to the possibility to integrate simulations and data coming from different models and sources. For an overview of different applications we suggest [22, 16, 40, 3, 4, 24]. A particularly promising nonlinear autoregressive multi-fidelity Gaussian process regression (NARGP), was proposed in [38]. Recent advancements in the context of physics informed neural networks [41] in a multi-fidelity setting for function approximation and inverse PDE problems, can be found in [31].

These models achieve increased expressiveness with some kind of nonlinear approach extending GP models to non-GP processes at the cost of an additional computational load. In this direction, some works aim to obtain computationally efficient heteroscedastic GP models using

*francesco.romor@sissa.it

†marco.tezzele@sissa.it

‡markus.mrosek@volkswagen.de

§carsten.othmer@volkswagen.de

¶gianluigi.rozza@sissa.it

a variational inference approach [27], or a nonlinear transformation [48]. This approach is extended to multi-fidelity models starting from the linear formulation presented by Kennedy and O’Hagan [22] towards deep GP [11] and NARGP.

Classical low-fidelity models obtained by coarse grids or simplified physical models still suffer the curse of dimensionality when used for high-dimensional GP construction. Linear parameter space reduction with Active Subspaces (AS) [8] can fight such curse using input-output couples obtained by high-fidelity simulations. Successful applications of parameter space reduction with active subspaces can be found in many engineering fields: naval and nautical problems [52], shape optimization [30, 17, 14, 12], car aerodynamics studies [35], inverse problems [10, 33], cardiovascular studies coupled with intrusive model order reduction [49], for the study of high-dimensional parametric PDEs [34], and in CFD problems in a data-driven setting [13, 50], among others. New extensions of AS have also been developed in the recent years such as AS for multivariate vector-valued functions [56], a kernel approach for AS for scalar and vectorial functions [42], a localization extension for both regression and classification tasks [43], and sequential learning of active subspaces [55]. The multi-fidelity setting has been used to find an active subspace given different fidelity models [25].

Other nonlinear techniques for parameter space reduction include manifold learning [20, 39], active manifolds [5] and nonlinear level-set learning (NLL) [57]. NLL adopts a Reversible Neural Networks (RevNet) architecture to learn an effective parameter space deformation to capture the geometry of the objective function level-sets and parametrize them.

With this contribution we show how to integrate linear and nonlinear parameter space dimensionality reduction within a multi-fidelity regression scheme based of Gaussian processes to increase the accuracy of high-dimensional response surfaces. The low-fidelity models are built with AS or NLL and incorporated in the NARGP framework, following the preliminary results obtained in [45]. An extensive automotive test case is presented with different configurations.

This work is organized as follows: in Section 2 we introduce multi-fidelity Gaussian process regression starting from the building block of a single fidelity up to the NARGP method; in Section 3 we focus on the parameter space reduction with active subspaces and nonlinear level-set learning which are going to be used to construct the low-fidelity models; Section 4 shows how to add the low-intrinsic dimensionality bias into the NARGP framework, accompanied by pseudocode; in Section 5 we present the numerical results of the proposed approach applied to two benchmark models, and to an automotive application; finally Section 6 draw the conclusions and some future research lines.

2 Multi-fidelity Gaussian process regression

In this section we are going to briefly recall the Gaussian process regression (GPR) technique in order to better characterize the nonlinear autoregressive multi-fidelity Gaussian process regression (NARGP) introduced in [38]. NARGP represents the main framework for our proposed multi-fidelity method. We are going to consider the general setting with multiple levels of fidelity.

2.1 Gaussian process regression

Gaussian process regression is a supervised technique to approximate unknown functions given a finite set of input/output pairs $\mathcal{S} = \{x_i, y_i\}_{i=1}^N$. Let $f : \mathcal{X} \subset \mathbb{R}^m \rightarrow \mathbb{R}$ be the scalar function of interest. The set \mathcal{S} is generated through f with the following relation: $y_i = f(x_i)$, which are the noise-free observations. We assigned a prior to f with mean $m(\mathbf{x})$ and covariance function $k(\mathbf{x}, \mathbf{x}'; \theta)$, that is $f(\mathbf{x}) \sim \mathcal{GP}(m(\mathbf{x}), k(\mathbf{x}, \mathbf{x}'; \theta))$. The prior expresses our beliefs about the function before looking at the observed values. From now on we consider zero mean \mathcal{GP} , that is $m(\mathbf{x}) = \mathbf{0}$, and we define the covariance matrix as $\mathbf{K}_{i,j} = k(x_i, x_j; \theta)$, with $\mathbf{K} \in \mathbb{R}^{N \times N}$. In order to make predictions using the Gaussian process we still need to find the optimal values for the hyper-parameters vector θ by maximizing the log likelihood:

$$\log p(\mathbf{y}|\mathbf{x}, \theta) = -\frac{1}{2}\mathbf{y}^T \mathbf{K}^{-1} \mathbf{y} - \frac{1}{2} \log |\mathbf{K}| - \frac{N}{2} \log 2\pi. \quad (1)$$

Let \mathbf{x}_* be the test samples, and $\mathbf{K}_{N*} = k(\mathbf{x}, \mathbf{x}_*; \theta)$ be the matrix of the covariances evaluated at all pairs of training and test samples, and in a similar fashion $\mathbf{K}_{*N} = k(\mathbf{x}_*, \mathbf{x}; \theta)$, and $\mathbf{K}_{**} =$

$k(\mathbf{x}_*, \mathbf{x}_*; \theta)$. By conditioning the joint Gaussian distribution on the observed values we obtain the predictions f_* by sampling the posterior as

$$f_* | \mathbf{x}_*, \mathbf{x}, \mathbf{y} \sim \mathcal{N}(\mathbf{K}_{*N} \mathbf{K}^{-1} \mathbf{y}, \mathbf{K}_{**} - \mathbf{K}_{*N} \mathbf{K}^{-1} \mathbf{K}_{N*}). \quad (2)$$

2.2 Nonlinear multi-fidelity Gaussian process regression

In this section we briefly present the nonlinear autoregressive multi-fidelity Gaussian process regression (NARGP) scheme [38]. It extends the concepts present in [22, 28] to nonlinear correlations between the different available fidelities.

The procedure is purely data-driven. We start from the input/output pairs corresponding to p levels of increasing fidelity, that is

$$\mathcal{S}_q = \{x_i^q, y_i^q\}_{i=1}^{N_q} \subset \mathcal{X} \times \mathbb{R} \subset \mathbb{R}^m \times \mathbb{R}, \quad \text{for } q \in \{1, \dots, p\}, \quad (3)$$

where $y_i^q = f_q(x_i^q)$. With p we indicate the highest fidelity. We also assume that the design sets have a hierarchical structure:

$$\pi(\mathcal{S}_p) \subset \pi(\mathcal{S}_{p-1}) \subset \dots \subset \pi(\mathcal{S}_1), \quad (4)$$

where $\pi : \mathbb{R}^m \times \mathbb{R} \rightarrow \mathbb{R}^m$ is the projection onto the first m coordinates. Due to this hierarchy, when the fidelities of the available datasets cannot be neatly assessed, it is reasonable to consider the cost needed to produce them as ordering criterion, see Remark 3.

The NARGP formulation assigns a Gaussian process to each fidelity model f_q , so they are completely defined by the mean field m_q , with the constant zero field as prior, and by their kernel k_q , as follows:

$$y_q(\bar{x}) - \epsilon \sim \mathcal{GP}(f_q(\bar{x}) | m_q(\bar{x}), k_q(\theta_q)) \quad \forall q \in \{1, \dots, p\}, \quad (5)$$

where $\epsilon \sim \mathcal{N}(0, \sigma^2)$ is a noise term and

$$\bar{x} := \begin{cases} (\mathbf{x}, f_{q-1}(\mathbf{x})) \in \mathbb{R}^m \times \mathbb{R}, & q > 1 \\ \mathbf{x} \in \mathbb{R}^m, & q = 1 \end{cases}. \quad (6)$$

The definition of the kernel $k_q(\theta_q)$ implements the auto-regressive characteristic of the method since it depends on the previous fidelity model f_{q-1} :

$$k_q((x, f_{q-1}(x)), (x', f_{q-1}(x')) | \theta_q) = k_q^\rho(x, x'; \theta_q^\rho) \cdot k_q^f(f_{q-1}(x), f_{q-1}(x'); \theta_q^f) + k_q^\delta(x, x'; \theta_q^\delta). \quad (7)$$

The hyper-parameters to be tuned are represented by $\theta_q \equiv (\theta_q^\rho, \theta_q^f, \theta_q^\delta)$ and are associated respectively to the multiplicative kernel k_q^ρ , the auto-regressive kernel k_q^f , and the kernel k_q^δ , which corresponds to the non auto-regressive part in the sum of Equation 7. For our applications we employ the radial basis function kernel with automatic relevance determination (RBF-ARD) [54], but there are other possible choices.

The presence of the multiplicative kernel k_q^ρ allows nonlinear interdependencies between subsequent fidelities to be modelled, surpassing a linear auto-regressive multi-fidelity scheme. The latent manifold that relates the inputs, the lower fidelity posterior and the high-fidelity posterior is in this case nonlinear [38].

We use the notation $(\mathbf{x}, y_{q-1}(\mathbf{x}))$ for the training set and \mathbf{x}_* for the new input. So in order to evaluate the predictive mean and variance for a new input \mathbf{x}_* we have to integrate the posterior $p(f_q(\mathbf{x}_*) | f_{q-1}, \mathbf{x}_*, \mathbf{x}_q, y_q)$ defined as

$$f_q(\mathbf{x}_* | f_{q-1}, \mathbf{x}_*, \mathbf{x}_q, y_q) \sim \mathcal{N}(\mathbf{K}_{*N}^q (\mathbf{K}^q)^{-1} y_q, \mathbf{K}_{**}^q - \mathbf{K}_{*N}^q (\mathbf{K}^q)^{-1} \mathbf{K}_{N*}^q), \quad (8)$$

$$\mathbf{K}_{*N}^q = k_q(\mathbf{x}_*, f_{q-1}(\mathbf{x}_*), (\mathbf{x}_{q-1}, y_{q-1}); \theta_q), \quad (9)$$

$$\mathbf{K}_{N*}^q = k_q((\mathbf{x}_{q-1}, y_{q-1}), (\mathbf{x}_*, f_{q-1}(\mathbf{x}_*)); \theta_q), \quad (10)$$

$$\mathbf{K}^q = k_q((\mathbf{x}_{q-1}, y_{q-1}), (\mathbf{x}_{q-1}, y_{q-1}); \theta_q), \quad (11)$$

over the Gaussian distribution of the prediction at the previous level $f_{q-1}(\mathbf{x}_*) \sim \mathcal{N}(m_{q-1}(\mathbf{x}_*), k_{q-1}(\mathbf{x}_*))$. Apart from the first level of fidelity $q = 1$ the posterior probability distribution given the previous

fidelity models is no longer Gaussian. So, in practice, the following integral is approximated with recursive Monte Carlo at each fidelity level, for all $q \in \{2, \dots, p\}$,

$$\begin{aligned} p(f_q^{\text{post}}(\mathbf{x}_*)) &:= p(f_q(\mathbf{x}_*)|f_{q-1}, \mathbf{x}_*, \mathbf{x}_q, y_q) = \\ &= \int_{\mathcal{X}} p(f_q(\mathbf{x}_*)|s, \mathbf{x}_*, \mathbf{x}_q, y_q) d\mathcal{L}_{f_{q-1}^{\text{post}}(\mathbf{x}_*)}(s) \end{aligned} \quad (12)$$

$$p(f_1^{\text{post}}(\mathbf{x}_*)) := p(f_1(\mathbf{x}_*)|\mathbf{x}_*, \mathbf{x}_1, y_1) \sim \mathcal{N}(m_1(\mathbf{x}_*), k_1(\mathbf{x}_*)), \quad (13)$$

where $\mathcal{L}_{f_{q-1}^{\text{post}}(\mathbf{x}_*)}$ is the probability law of $f_{q-1}^{\text{post}}(\mathbf{x}_*) \sim \mathcal{N}(m_{q-1}(\mathbf{x}_*), k_{q-1}(\mathbf{x}_*))$. In the applications we always use 200 to 10000 Monte Carlo samples, since the results do not vary much increasing them for our test cases.

The hyper-parameters θ_q are optimized (non recursively) with maximum log-likelihood estimation for each GP model $\mathcal{GP}(f_q|\mathbf{0}, k^q(\theta_q))$, for all $q \in \{1, \dots, p\}$,

$$\underset{\theta_q}{\text{argmin}} -\log p(f_q(\mathbf{x}_q)|\mathbf{x}_q, y_q, y_{q-1}, \theta_q) \propto \frac{1}{2} \log |K^q(\theta_q)| + \frac{1}{2} y_q^T (K^q(\theta_q))^{-1} y_q,$$

this is why a hierarchical dataset is needed. The hyperparameters tuning is achieved maximizing the log-likelihood with the gradient descent optimizer L-BFGD in GPy [18]. For some test cases, the training procedure is subject to relevant perturbations relative to the number of restarts, this is especially true in higher dimensions of the parameter space.

3 Parameter space reduction

Our aim is testing multi-fidelity Gaussian process regression models to approximate objective functions which depend on inputs/parameters sampled from a high-dimensional space. Low-fidelity models relying on a physics-based or numerical model reduction — for example a coarse discretization or a more specific numerical model order reduction — still suffer from the high dimensionality of the input space. In our approach we try to tackle these problematics by searching for a surrogate (low-fidelity) model accounting for the complex correlations among the input parameters that concur to the output of interest. With this purpose in mind, in this section we are going to briefly present the active subspaces (AS) [8], and the nonlinear level-set learning (NLL) method [57] for parameter space reduction in order to design response surfaces with Gaussian process regression.

3.1 Active subspaces

Let \mathbf{X} be an absolutely continuous random variable with probability density ρ , such that $\text{supp}(\rho) = \mathcal{X} \subset \mathbb{R}^m$. The variable \mathbf{X} represents the inputs, and m denotes the dimension of the input parameter space. With simple Monte Carlo we can approximate the uncentered covariance matrix of the gradients of the function of interest as

$$\mathbb{E}_\rho[\nabla_{\mathbf{x}} f (\nabla_{\mathbf{x}} f)^T] \approx \frac{1}{N} \sum_{i=1}^N \nabla_{\mathbf{x}} f(\mathbf{X}_i) (\nabla_{\mathbf{x}} f(\mathbf{X}_i))^T, \quad (14)$$

where N denotes the number of samples. We are looking for the highest spectral gap $\lambda_r - \lambda_{r+1}$ in the sequence of ordered eigenvalues of the approximated correlation matrix. The active subspace is the eigenspace corresponding to the first r eigenvalues $\lambda_1, \dots, \lambda_r$ and it is denoted with the matrix $\hat{W}_r \in \mathcal{M}(m \times r)$ whose columns are the corresponding r active eigenvectors. The inactive subspace is defined as the span of the remaining eigenvectors. On it f is almost flat on average, so we can safely discard such component without compromising too much the accuracy. We can thus build a response surface \mathcal{R} using a Gaussian process regression trained with N_{train} pairs $\{\hat{W}_r^T \mathbf{x}_i, y_i\}_{i=1}^{N_{\text{train}}}$ of active inputs and outputs.

The mean square regression error is bounded a priori [8] by

$$\mathbb{E}_\rho \left[(f(\mathbf{X}) - \mathcal{R}(\hat{W}_r^T \mathbf{X}))^2 \right] \leq C_1 (1 + N^{-1/2})^2 \left(\epsilon (\lambda_1 + \dots + \lambda_r)^{1/2} + (\lambda_{r+1} + \dots + \lambda_m)^{1/2} \right)^2 + C_2 \delta, \quad (15)$$

where C_1 and C_2 are constants, ϵ quantifies the error in the approximation of the true active subspace W_r with \hat{W}_r obtained from the Monte Carlo approximation, and $C_2\delta$ is a bound on the mean squared error of the Gaussian process regression over the active subspace:

$$\mathbb{E}_{\rho_{\hat{W}_r, \mathbf{X}} | \hat{W}_{m-r}, \mathbf{X}} \left[\left(\overline{\mathbb{E}_{\rho} [f(\mathbf{X}) | \sigma(\hat{W}_r^T \mathbf{X})]} - \mathcal{R}(\hat{W}_r^T \mathbf{X}) \right)^2 \right] \leq C_2 \delta, \quad (16)$$

where $\rho_{\hat{W}_r, \mathbf{X} | \hat{W}_{m-r}, \mathbf{X}}$ is the probability of the active variables conditioned on the inactive ones, and $\overline{\mathbb{E}_{\rho} [f(\mathbf{X}) | \sigma(\hat{W}_r^T \mathbf{X})]}$ is the random variable $f(\mathbf{X})$ conditioned on the σ -algebra generated by $\hat{W}_r^T \mathbf{X}$ and approximated with the Monte Carlo method.

3.2 Nonlinear level-set learning method

This method seeks a bijective nonlinear transformation $g_{\text{NLL}} : \mathcal{X} \rightarrow \tilde{\mathcal{X}} \subset \mathbb{R}^m$ to capture the geometry of level sets and parametrize them in a low-dimensional space. To this end in [57] they employ reversible networks (RevNets) [6] to learn the transformation g_{NLL} . The designed loss function uses samples of the gradients of the target function to encourage the transformed function to be sensitive to only a few active coordinates.

To construct the RevNet, the following architecture [19], which is reversible by definition, is employed:

$$\begin{cases} u_{n+1} = u_n + hK_{n,1}^T \sigma(K_{n,1} v_n + b_{n,1}), \\ v_{n+1} = v_n - hK_{n,2}^T \sigma(K_{n,2} u_n + b_{n,2}), \end{cases} \quad \text{for } n = 0, 1, \dots, N-1, \quad (17)$$

where u and v are partitions of the states, h is a scalar time step, the matrices K contain the weights, b represent the biases, and σ is the activation function. We remark that the original coordinates and the transformed ones are split in two in u and v .

4 Multi-fidelity data fusion with active subspaces

Our study regards the design of a nonlinear autoregressive multi-fidelity Gaussian process regression (NARGP) [38] with two fidelities: the high-fidelity corresponds to a relatively accurate and costly model, for example a numerical model which requires computationally intensive simulations to obtain a scalar output for each parameter sample; and the low-fidelity level which comes from a response surface built through a parameter space reduction technique — here we focus on active subspaces but little modifications are required in order to use NLL as we are going to show. We consider models with high-dimensional input space but with a low intrinsic dimensionality. This setting characterizes many industrial applications [35, 52, 30].

In fact, the inductive biases we impose come mainly from two sources: the kernel of the Gaussian process (lengthscale, noise, regularity of the stochastic process) and the low-fidelity intrinsic dimensionality assumption (presence of a dominant linear or nonlinear active subspace). The key feature of the method is the imposition of the latter on the multi-fidelity model design: we expect that a hint towards the presence of an active subspace will be transferred from the low-fidelity to the high-fidelity level through the discovery of nonlinear correlations between the low-fidelity predictions, and the high-fidelity inputs/outputs dataset. In this way, the accuracy should increase in the data-scarcity regime, i.e. when the number of high-fidelity samples are not enough to obtain an accurate single-fidelity regression. The overhead with respect to the original procedure [38] is the evaluation of the active subspace from the high-fidelity inputs and the training of the whole multi-fidelity model; this costs are usually negligible as shown in section 5.2.

In Figure 1 we present an illustrative scheme of the proposed NARGP-AS method; the underlying objective function is an hyperbolic paraboloid $f : [0, 1]^2 \subset \mathbb{R}^2 \rightarrow \mathbb{R}$, $f(x_1, x_2) = x_1^2 - x_2^2$ and is shown only for the purpose of representing the procedure more clearly. The high-fidelity flow field belongs to the automotive application of section 5.2.

For clarity we will use the letters H and L as labels for the high-fidelity and low-fidelity models respectively, instead of the fidelity levels $q = 1$ and $q = 2$. Changing, as just described, the

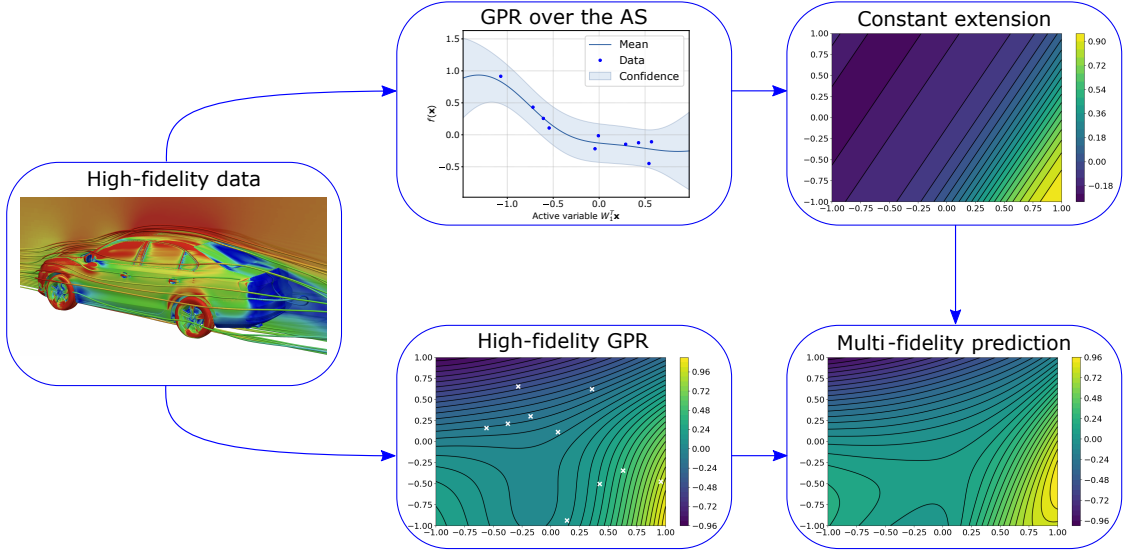


Figure 1: Illustrative scheme of the NARGP-AS method. Starting from 10 high-fidelity data (depicted with blue dots and white crosses) we construct as low-fidelity model a response surface which is constant along the inactive subspace.

notations of subsection 2.2, we consider

$$S^L = \{x_i^L, y_i^L\}_{i=1}^{N_L} \subset \mathbb{R}^m \times \mathbb{R},$$

$$S^H = \{x_i^H, y_i^H\}_{i=1}^{N_H} \subset \mathbb{R}^m \times \mathbb{R},$$

and additionally $\{dy_i^H\}_{i=1}^{N_H} \subset \mathbb{R}^m$ the gradients corresponding to the high-fidelity dataset $S^H = \{x_i^H, y_i^H\}_{i=1}^{N_H}$: in principle, the gradients can be directly obtained from the model of interest (with adjoint methods in case of PDE models for example) or approximated from the input output pairs S^H . For the influence of the gradients' approximation on the regression error, see [8]. For our test cases we employ the exact gradients when available (for the benchmarks in sections 5.1.1 and 5.1.2) or we approximate them from the high-fidelity GPR (in the test cases in sections 5.2.1, 5.2.2 and 5.2.3). This does not results in additional costs, since the HF GPR is needed in the NARGP-AS procedure.

The high-fidelity dataset S^H (and the corresponding gradients) represents by itself all the necessary ingredients: S^L is built from S^H through a response surface on the linear or nonlinear active subspace. For this purpose the dataset S^H is employed, with the corresponding gradients, to find an active subspace \hat{W}_r or train a RevNet, as described in subsections 3.1 and 3.2.

Then, since $S^H \subset S^L$, we write

$$S^L \setminus S^H = \{x_i^L, y_i^L\}_{i=1}^{N_L} \setminus \{x_i^H, y_i^H\}_{i=1}^{N_H} = \{\tilde{x}_i^L, \tilde{y}_i^L\}_{i=1}^{N_L - N_H}. \quad (18)$$

The additional low-fidelity inputs $\{\tilde{x}_i^L\}_{i=1}^{N_L - N_H}$ are sampled independently from the inputs' probability distribution, while the additional low-fidelity outputs $\{\tilde{y}_i^L\}_{i=1}^{N_L - N_H}$ are the predictions associated to the active components of the additional low-fidelity inputs $\{\hat{W}_r^T \tilde{x}_i^L\}_{i=1}^{N_L - N_H}$, obtained from the response surface trained on

$$\{\hat{W}_r^T x_i^H, y_i^H\}_{i=1}^{N_H} \subset \mathbb{R}^r \times \mathbb{R}.$$

The response surface is trained as a Gaussian process regression as described in subsection 3.1. The procedure is synthetically reviewed through Algorithm 1. The number of low-fidelity samples is chosen until a good approximation of the low-fidelity response surface is obtained. As it is experimentally shown in Figure 8, additional low-fidelity samples do not improve the accuracy of the multi-fidelity model afterwards.

Remark 1 (Nonlinear level-set learning as LF model). If NLL is employed to build the low-fidelity level, only the first step of Algorithm 1 is changed. For our applications, the GPR designed with NLL has dimension one.

Algorithm 1: NARGP-AS response surface design algorithm.

input : training high-fidelity inputs, outputs, gradients triplets

$$\{(\mathbf{x}_i^H, y_i^H, dy_i^H)\}_{i=1}^{N_H} \subset \mathbb{R}^m \times \mathbb{R} \times \mathbb{R}^m,$$
$$\text{low-fidelity inputs } \{\mathbf{x}_i^L\}_{i=1}^{N_L} \subset \mathbb{R}^m,$$

output: multi-fidelity model,

$$((f_H|x_i^H, y_i^H), (f_L|x_i^L)) \sim (\mathcal{GP}(f_H|m_H, k_H), \mathcal{GP}(f_L|m_L, k_L))$$

- 1 Compute the active subspace \hat{W}_r with the high-fidelity gradients $\{dy_i^H\}_{i=1}^{N_H}$,
 - 2 Build the response surface $\mathcal{R}(\hat{W}_r, \mathbf{X})$ with a GP regression from $\{(\hat{W}_r \mathbf{x}_i^H, y_i^H)\}_{i=1}^{N_H}$,
 - 3 Predict the low-fidelity outputs $\{y_i^L\}_{i=1}^{N_L}$ at $\{\mathbf{x}_i^L\}_{i=1}^{N_L}$ and the training high-fidelity inputs $\{y_i^H\}_{i=1}^{N_H}$ at $\{\mathbf{x}_i^H\}_{i=1}^{N_H}$ with the response surface,
 - 4 Train the multi-fidelity model at the low-fidelity level f_L with the training dataset $\{(x_i^L, y_i^L)\}_{i=1}^{N_L} \cup \{(x_i^H, y_i^H)\}_{i=1}^{N_H}$,
 - 5 Train the multi-fidelity model at the high-fidelity level f_H with the training dataset $\{(x_i^H, y_i^H)\}_{i=1}^{N_H}$
-

Remark 2 (Markov property). Theoretically the observations $\{y_i^q\}$ should be noiseless for each level of fidelity q in order to preserve the Markov property [38]. However, in practice, it could be beneficial in some applications to add noise at each fidelity level, or constraint the noise levels from below in order to avoid overfitting.

5 Numerical results

In this section we are going to present the results obtained with the NARGP-AS and the NARGP-NLL method over two benchmark test problems (Piston 5.1.1 and Ebola 5.1.2 models), and over a more complex car aerodynamics problem (Jetta-6 5.2.1, Jetta-12-RANS 5.2.2, Jetta-12-DDES 5.2.3). The library employed to implement the NARGP model is Emukit [36] while for the active subspace and NLL response surface design we used the open source Python package¹ called ATHENA [44], and GPy [18].

The computational times of the prediction and training of the NARGP-AS method are reported in Table 1. In particular, it is shown how the number of HF test samples and of Monte Carlo (MC) samples affect the MF prediction times. The training costs are mainly affected by the number of restarts of the optimization with L-BFGD, instead.

Table 1: Computational times of the training of the multi-fidelity models and evaluation of the predictions.

Test Case	# HF Training Samples	Training	Restarts	MC Samples	# HF Test Samples	MF Prediction	HF Prediction
Piston model 5.1.1	150	24 [s]	10	100	10000	10 [s]	0.123 [s]
Ebola model 5.1.2	150	21 [s]	10	100	10000	10 [s]	0.450 [s]
Jetta-6 5.2.1	76	229 [s]	150	100	25	0.056 [s]	0.0006 [s]
Jetta-12-RANS 5.2.2	185	50 [s]	10	10000	51	14.2 [s]	0.0006 [s]
Jetta-12-DDES 5.2.3	65	20 [s]	10	1000	50	0.02 [s]	0.0003 [s]

5.1 Benchmark test problems

The first benchmark test problem presents a 7-dimensional input parameter space and the quantity of interest is the time a cylindrical piston takes to complete a cycle². The second one is a 8-dimensional model for the spread of Ebola in Western Africa [15]. These tests have been chosen because of the presence of an active subspace and they indeed present a low intrinsic dimensionality. The sufficient summary plot is plotted for both the cases together with a one-dimensional Gaussian

¹Available at <https://github.com/mathLab/ATHENA>.

²The piston dataset was taken from https://github.com/paulcon/active_subspaces.

process regression built over the AS. We also show the correlation between the low-fidelity level and the high-fidelity level of the multi-fidelity model. We compare the performance of the different fidelities looking at the corresponding R^2 scores. This score is chosen to show how the obtained regressions compare with respect to a constant predictor equal to the function average ($R^2 = 0$). With LF we denote the low-fidelity model represented by a GP regression on the low-fidelity input/output couples, with HF the high-fidelity model represented by a GP regression built on the full space, and with MF the proposed multi-fidelity model. The number of low-fidelity samples is kept fixed at 200 for both test cases, while we study the accuracy varying the number of high-fidelity training samples used. For both the benchmark problems the models were tested over a dataset comprising 10000 samples, selected with Latin hypercube sampling (LHS). The nonlinear autoregressive fidelity fusion approach achieves better performance with a consistent increase in the R^2 score.

5.1.1 The piston model

For this model the scalar target function of interest represents the time it takes the piston to complete a cycle, depending on a 7-dimensional parameters vector. For its evaluation a nonlinear function has to be computed. The input parameters are uniformly distributed. For a detailed description of the parameters' ranges the reader can refer to [9]. The algebraic cylindrical piston model appeared as a test for statistical screening in [2], while in [9] they describe an active subspaces analysis.

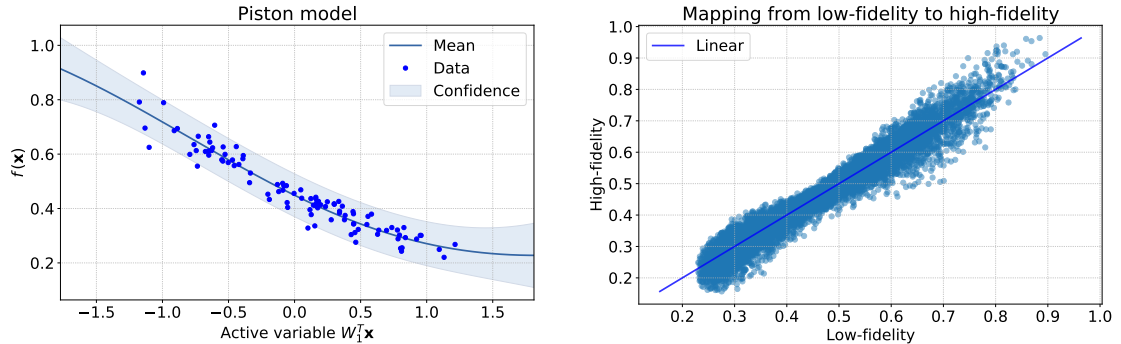


Figure 2: Left: sufficient summary plot of the surrogate model built with active subspaces. 100 samples were used to build the AS surrogate model shown. Right: correlations among the low-fidelity level and the high-fidelity level of the multi-fidelity model, evaluated at the 10000 test samples.

From the sufficient summary plot reported in the left panel of Figure 2 we can conclude that a one-dimensional active subspace is able to describe the input-output dependency with a sufficient accuracy. This is also supported by the GPR built over the AS. Moreover, the ordered eigenvalues of the covariance matrix of the gradients exhibit a spectral gap between the first and the second eigenvalue. In the right panel of Figure 2 we present the correlation between the high- and low-fidelity of the NARGP model.

Figure 3 shows on the left the mean R^2 scores of the MF model built as described in Section 4 varying the number of high-fidelity data. This is done over 10 training restarts of the MF, LF and HF models: moreover each GPR training is restarted 10 times for the HF and LF models and 20 times for the MF model at each fidelity level, inside the GPy package. We show also the minimum and maximum R^2 scores over the outer 10 training restarts to show the stability of the procedure. When we have a scarce amount of data the models are not so robust as we can see in the left part of the plot for 50 and 60 high-fidelity samples. After that point we have very stable results which account for a relative gain in the 3-5% range with respect to the high-fidelity regression.

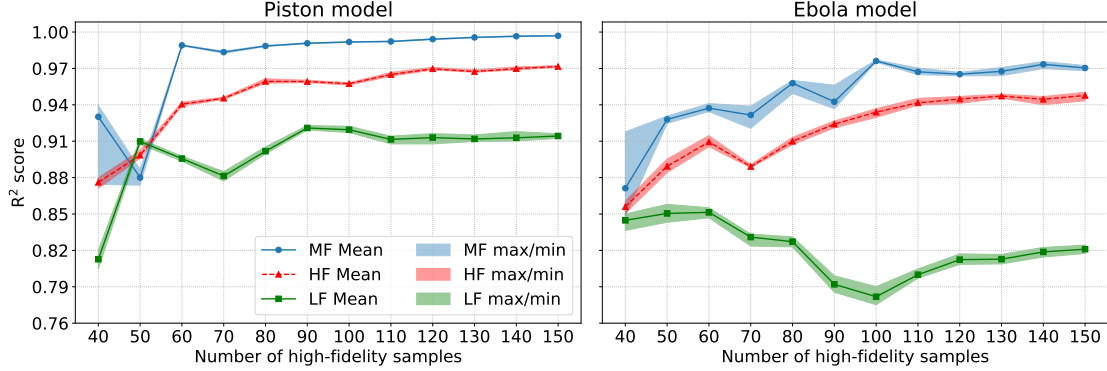


Figure 3: R^2 score of the posterior of the multi-fidelity (MF), high-fidelity (HF) and low-fidelity (LF) models against the number of high-fidelity samples used to find the active subspace and build the Gaussian process regressions of the MF, HF, LF models. The 10000 test samples are distributed with Latin hypercube sampling (LHS). In the left panel the results for the piston model, while on the right the Ebola spread model.

5.1.2 Modified SEIR model for Ebola

Now we consider the modified SEIR model for the spread of Ebola in Liberia, presented in [15], which depends on 8 parameters. As scalar output of interest we take the basic reproduction number R_0 . It can be computed with the following formula:

$$R_0 = \frac{\beta_1 + \frac{\beta_2 \rho_1 \gamma_1}{\omega} + \frac{\beta_3}{\gamma_2} \psi}{\gamma_1 + \psi}, \quad (19)$$

with parameters range taken from [15], where they conducted a global sensitivity analysis with AS. For a kernel-based active subspaces comparison the reader can refer to [42].

In this case a one-dimensional Gaussian process response surface is not able to achieve the same good accuracy of the previous case, as can be seen in the left panel of Figure 4. This is also confirmed by the correlation between the low- and high-fidelity levels of the NARGP, depicted in the right panel of Figure 4. The corresponding R^2 scores in the right panel of Figure 3 reflect this behaviour of worse performance with respect to the piston test case, where better correlations among the fidelities were identified. The relative gain is in the 3–4% range with respect to the high-fidelity regression.

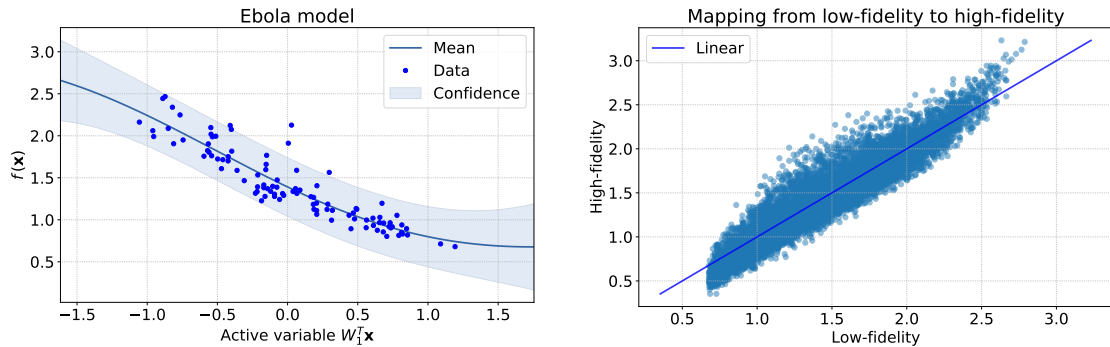


Figure 4: Left: sufficient summary plot of the Ebola model, 100 samples were used to build the AS surrogate model shown. Right: correlations among the low-fidelity level and the high-fidelity level of the multi-fidelity model, evaluated at the 10000 test samples.

5.2 Automotive application

Two different test cases from the world of automotive aerodynamics are investigated in order to demonstrate the applicability of the presented method to real-life problems. The first one (named hereafter **Jetta-6**) is taken from [32], where it is described in detail. It consists of a 6-dimensional geometric parameterization of the Volkswagen Jetta VI. The parameters (see Table 2) were generated by free-form deformation and focus on the rear part of the car. A Latin Hypercube with 101 samples was created, and the aerodynamic flow fields were computed with OpenFOAM [53] via Delayed Detached Eddy Simulations (DDES). An illustrative example can be seen in Figure 5. The physical simulation time was four seconds, and the fields were averaged over the last two seconds before integrating them over the vehicle surface to obtain the drag coefficient c_D . With mesh sizes being of the order of 100M cells, each variant required about 23,000 CPU-core-hours.

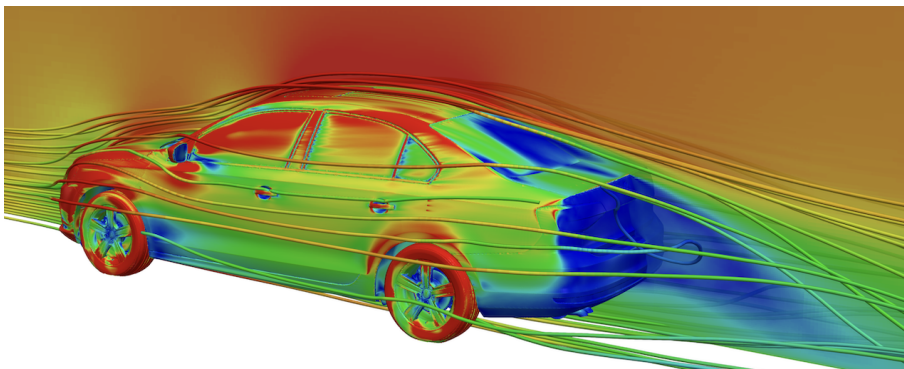


Figure 5: Visualization of the averaged flow field around the Jetta.

Table 2: Parameters' description of the Jetta-6 test case [32].

Parameter	Description	Lower bound	Upper bound
μ_1	Rear roof lowering	0 mm	50 mm
μ_2	Trunk height	-30 mm	30 mm
μ_3	Trunk length	-50 mm	100 mm
μ_4	Rear lateral tapering	-60 mm	50 mm
μ_5	Rear end edge position	-70 mm	30 mm
μ_6	Rear end depression	-15 mm	0 mm

The second automotive test case (named hereafter **Jetta-12**) is based on the same car model and was created within the EC project UPSCALE [1]. The parameterization consists of 12 geometric modifications all around the vehicle (see Figure 6 and Table 3). Besides the baseline geometry, a Sobol sequence of 300 additional samples was created and computed with OpenFOAM. To reduce the required computational budget to an affordable amount, Reynolds-Averaged-Navier-Stokes (RANS) computations were carried out instead of DDES runs. This allowed to use coarser meshes of 52M cells and resulted in 1700 CPU-core-hours for a single run for the 4000 iterations, of which the last 1000 were averaged to obtain the drag coefficient c_D .

In Figure 7 we depicted the eigenvalues decay for the automotive test cases. The largest spectral gap is always between the first and the second eigenvalue. This justifies the choice of a low-fidelity model built from a one-dimensional regression.

5.2.1 Multi-fidelity response surface design Jetta-6

In this test case, the low-fidelity model chosen is the response surface trained on the active latent variables obtained with the NLL method: instead of prolonging along the orthogonal directions the

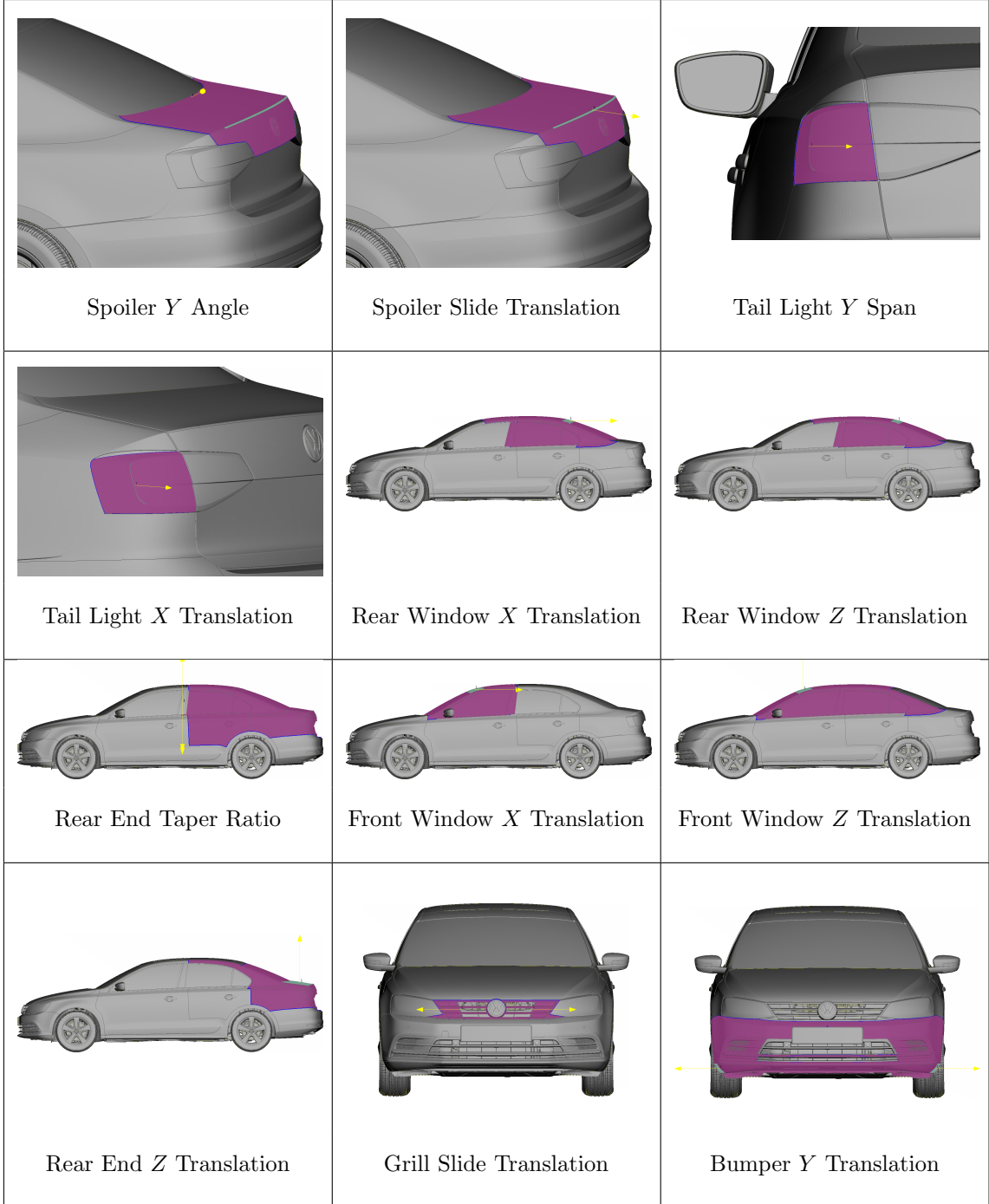


Figure 6: Affected areas by the geometrical parameters for the Jetta-12 test case. The ranges of each parameter can be gleaned from Table 3.

one-dimensional regression built on the active subspace, a GPR is trained on the deformed high-fidelity inputs $\{g_{\text{NLL}}(\mathbf{x}_i^H)\}_{i=1}^{N_H} \subset \tilde{\mathcal{X}}$. We remark that the map g_{NLL} does not preserve in general convexity of the domain \mathcal{X} or orthogonality of the boundaries. Nonetheless, this is not problematic for this application since we are not interested in backmapping the active latent variables from $\tilde{\mathcal{X}}$ to \mathcal{X} , but only in forwarding the inputs from \mathcal{X} to $\tilde{\mathcal{X}}$ and then evaluating the predictions with the GPR.

The employed RevNet has 10 layers. It was trained for 20000 epochs on a dataset of 76 training samples and 25 test samples, with ADAM stochastic optimization method [23], with an initial learning rate of 0.03. The high-fidelity samples were obtained with LHS method. The architecture is implemented in PyTorch [37] inside the ATHENA [44] Python package. We perform a study on

Table 3: Parameters' description of the Jetta-12 test case.

Parameter	Description	Lower bound	Upper bound
μ_1	Spoiler Y Angle	-5.0°	0.0°
μ_2	Spoiler Slide Translation	0.0 mm	30.0 mm
μ_3	Tail Light Y Span	-15.0 mm	5.0 mm
μ_4	Tail Light X Translation	-10.0 mm	10.0 mm
μ_5	Rear Window X Translation	-100.0 mm	100.0 mm
μ_6	Rear Window Z Translation	-30.0 mm	0.0 mm
μ_7	Rear End Taper Ratio	-1.0°	3.0°
μ_8	Front Window X Translation	-100.0 mm	100.0 mm
μ_9	Front Window Z Translation	-30.0 mm	0.0 mm
μ_{10}	Rear End Z Translation	-30.0 mm	30.0 mm
μ_{11}	Grill Slide Translation	-50.0 mm	50.0 mm
μ_{12}	Bumper Y Translation	-20.0 mm	20.0 mm

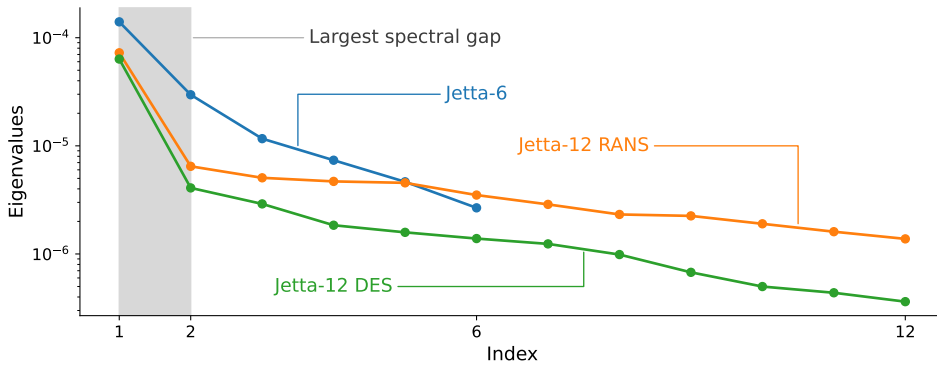


Figure 7: Eigenvalues decay of the covariance matrix of the gradients for the Jetta-6 and Jetta-12 test cases.

the number of additional LF samples, distributed uniformly on the domain, from 100 to 400 with a step of 50. The results are shown in Figure 8.

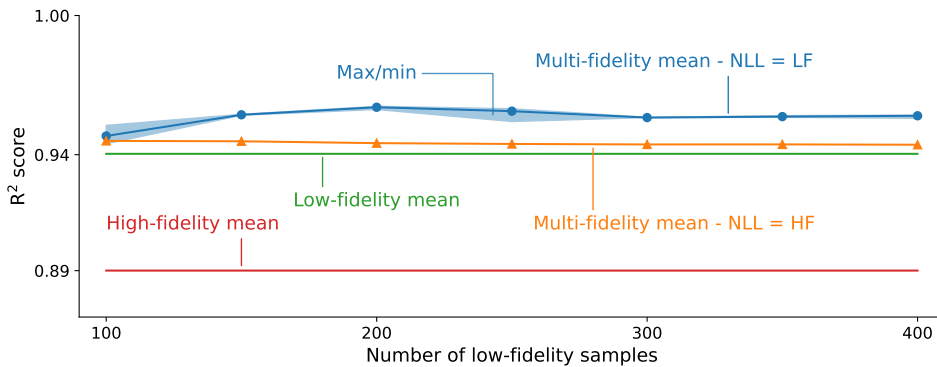


Figure 8: R^2 score evaluated on the 25 test samples obtained from LHS on the domain \mathcal{X} , varying the number of LF samples. The mean R^2 score over 10 restarts of the training of the GPR is shown. For the MF also the minimum and maximum values are reported. The orange line identifies the results obtained by reversing the fidelities order, so the number of LF samples corresponds to the HF GPR. The LF and HF R^2 scores are not influenced by the number of additional LF samples.

The maximization of the log-likelihood is performed with 10 restarts for the HF and LF models, and 100 restarts for the MF model, all inside GPy optimization algorithm. All training procedures are moreover restarted 10 times, testing the stability of the optimization process for each fidelity

model. This is done in order to show, in Figure 8 with blue lines, that the MF training presents some small instabilities with respect to the HF and LF training, as expected. The LF and HF models are designed over the same HF inputs-outputs datasets, so they are not influenced by the additional LF samples.

Remark 3 (Reversing the fidelities order). A natural question that may arise regards the correct ordering of the HF and LF models in the MF when the accuracy is higher for the LF as in Figure 8. We perform a study with respect to the number of additional samples from the HF GPR (not from the numerical simulations), now the lowest fidelity in the MF model. Moreover, in order to reach a desirable accuracy, we add to each of the 2 levels of fidelity of the MF model 200 uniformly sampled input-output pairs: the highest fidelity is the NLL GPR built with $76 + 200$ training data; the lowest fidelity is the HF GPR built with training data equal to 76 from numerical simulations $+200$ fictitiously from the HR GPR (not from numerical simulations) $+$ additional samples from 100 to 400 with a step of 50 from HR GPR (not numerical simulations). The results are reported in Figure 8 with orange lines (NLL = HF). The R^2 score is lower than the previous case. Generally, the ordering of the fidelities depends on the availability of data and the cost for obtaining them.

We also perform cross-validation (CV) with leave-one-out strategy for the Jetta-6 test case to assess the robustness of the result with respect to the test dataset, in Figure 9. We reported the mean and confidence intervals at 95% among the 25 batches of the leave-one-out strategy for a test set of 25 samples: each batch has 24 test samples. For each abscissa, the batches corresponding to the lowest R^2 score for the MF and highest R^2 score for the LF are found, so that with respect to these two selected batches the R^2 scores of the LF and MF models, respectively, can be computed and compared: we want to remark that batch-wise the MF R^2 score is always higher to the LF R^2 score.

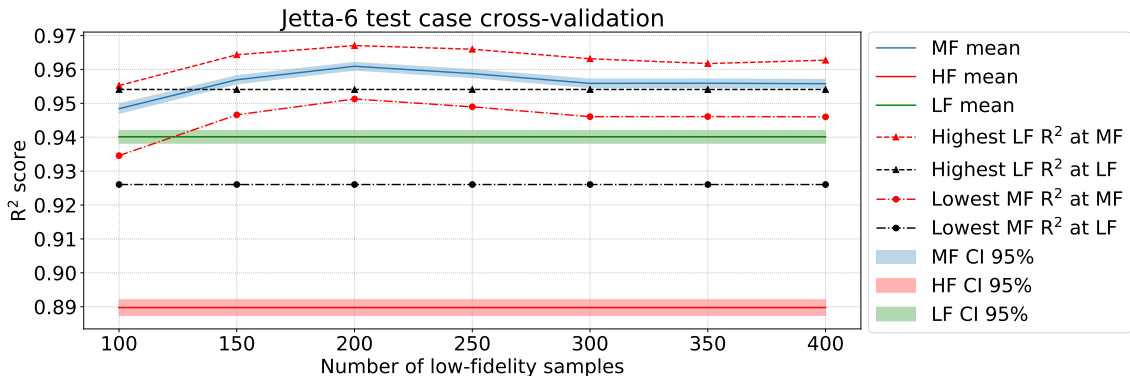


Figure 9: Cross-validation with leave-one-out strategy and confidence bounds at 95%. The labels **lowest MF R^2 at LF** stands for the R^2 score of the batch associated to the lowest R^2 score for the MF model in the CV procedure, but evaluated at the predictions of the LF model. The other labels are analogue.

5.2.2 Multi-fidelity response surface design Jetta-12

For this test case with additional 6 parameters with respect to the previous one, for a total of 12, a one-dimensional NLL response surface does not perform better than a one-dimensional AS response surface, so we preferred the latter as LF model. In this case we also added Gaussian noise at each fidelity level in order to achieve a better accuracy, loosing the Markov property, see Remark 2. Moreover, to avoid overfitting we restricted the variance of the Gaussian noise to the interval $[0.01, 0.1]$ at each fidelity of the multi-fidelity model.

We perform a study on the number of high-fidelity samples from 45 to 225, obtained from a Sobol' sequence. The test set has 51 samples obtained with LHS instead. The number of additional LF samples is 100. The results are reported in Figure 10. As for the Jetta-6 test case, we perform 10 outer training restarts for the LF, HF, and MF models: the 100 additional LF samples are resampled every time. Moreover, the optimization procedures of the GPRs are restarted 10 times for the LF, HF, and MF model. We employed also a validation dataset of additional independent 25 samples from the continuation of the Sobol' sequence: the markers in Figure 10 correspond

to the best HF and MF models with respect to the validation set. We also report maximum and minimum R^2 scores for the outer loop training restarts of the MF model to show that the validation process is fairly effective, at least when employing 45 to 155 high-fidelity samples. We emphasized in the plot the three distinct areas corresponding to the scarce data, low data, and abundance of data regimes.

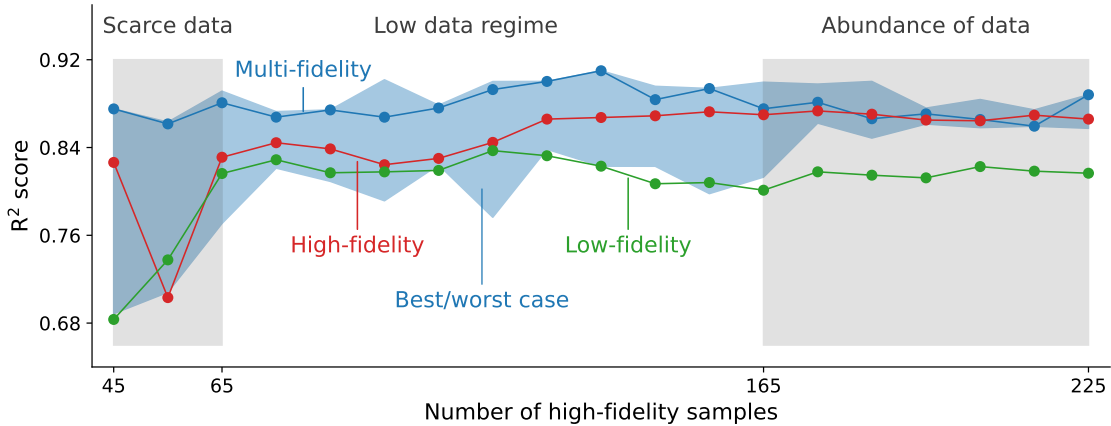


Figure 10: Jetta-12: R^2 score evaluated on the 51 test samples obtained from LHS on the domain \mathcal{X} , varying the number of HF samples. The mean R^2 score over 10 restarts of the training of the GPR is shown. For the MF model the minimum and maximum values are shown, differently from the HF and LF models, since the perturbations are not sensible. The markers associated to the MF and HF models represent the R^2 scores on the test set of the best HF and MF models with respect to an independent validation set of 25 samples.

It can be seen a gain of around 4% on average on the R^2 score of the MF model, with respect to the other two, in the abscissae range from 45 to 155. This time the procedure is much less stable with respect to the optimization process, probably due to the higher dimension of the input space. The decreasing behaviour of the R^2 score of the MF models from the abscissa 135 to 225 can be ascribed to the prevalence of the HF model: in this case the LF model influences less the predictions of the MF model, which are more stable and close to the HF ones. The low HF R^2 score at abscissa 55 is almost constant for each outer training step and is not related to overfitting, but it can be associated to a high sensitivity of the regression when employing a small dataset relative to the problem at hand.

We want also to remark that in this test case the training of the LF, HF, and MF models takes less than 10 minutes for each number of high-fidelity samples, with increasing costs from 45 to 225 samples, considering altogether the outer loop training restarts. Compared with the costs for a high-fidelity simulation, the MF training cost is negligible.

5.2.3 High-fidelity model choice for Jetta-12

In principle, any model of the same phenomenon originated from a different physical approximation, numerical method, or discretization, can be employed to produce a multi-fidelity model. In the case of the Jetta-12 automotive testcase, computations can be carried out with the more accurate DDES runs, as in the Jetta-6 testcase. Then, we have 3 models at our disposal: the response surfaces built on the DDES outputs, RANS outputs, or AS predictions.

We train the DDES-AS and DDES-RANS two-fidelity models as described in Section 2, and consider also the DES and AS single fidelity models. We compute 75 DDES training input-output pairs, and 50 DDES test input-output pairs, both sampled with LHS. Since the DDES simulations represent the highest fidelity, the DDES test samples will be used to evaluate the R^2 scores of all the other single and multi-fidelity models considered. All the 300 RANS training data available from the previous test case will be employed for the DDES-RANS model, and 100 additional LHS sampled input-output pairs obtained from the AS response surface will be used to train the DDES-AS two-fidelity model.

The R^2 errors on the test set are reported in Figure 11. Also in this case we use cross-validation with leave-one-out and leave-two-out strategy to assess the robustness of the results with respect to the test set: we show the mean, minimum, maximum, and standard deviation (std) with respect to the sets of $50 = \binom{50}{1}$ and $1225 = \binom{50}{2}$ cross-validation batches. When the two models are integrated in the DDES-AS MF model, the accuracy sensibly rises as observed in the previously. Only for the MF model, we extracted 10 validation samples from the 75 training dataset, so we trained it with exactly 65 samples and selected the best model looking at the R^2 score of the validation set. The effectiveness of the validation procedure is shown in Figure 12. Also in this case, we constrained the Gaussian noise levels of the MF model to belong to the interval $[0.01, 0.1]$.

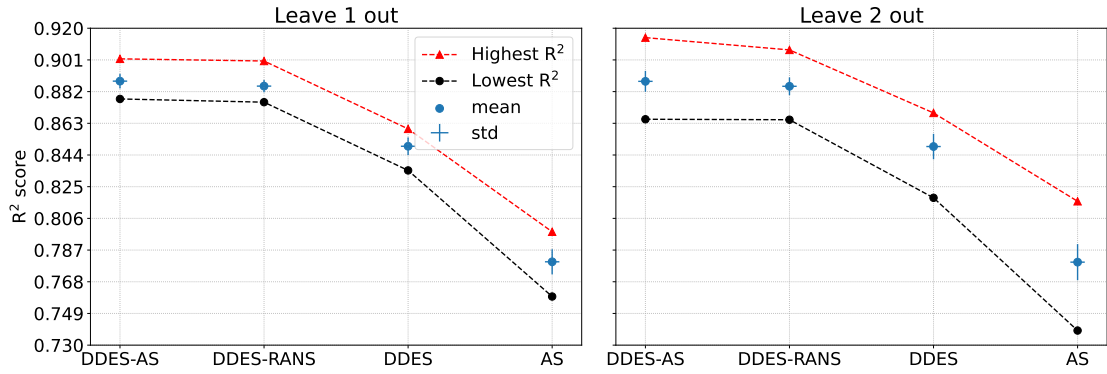


Figure 11: Cross-validation (CV) with leave-one-out (Left) and leave-two-out strategy (Right) on the test set. The labels **Lowest R^2** and **Highest R^2** stand for the R^2 score of the batch associated to the lowest and highest R^2 score, respectively. The mean and standard deviation shown (std) are computed with respect to the sets of $50 = \binom{50}{1}$ and $1225 = \binom{50}{2}$ cross-validation batches, respectively.

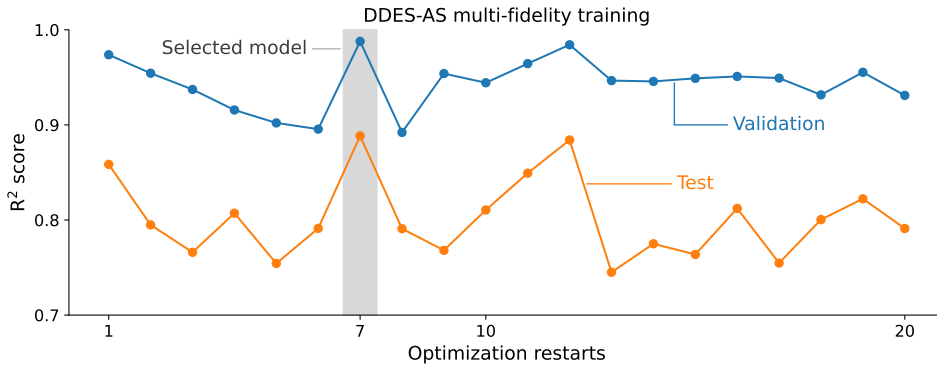


Figure 12: Validation process of the DDES-AS multi-fidelity model over 20 outer training restarts changing every time the additional 100 additional low-fidelity samples. The selected multi-fidelity model corresponds to abscissa 7.

The accuracy is comparable to the DDES-RANS MF model, implying that the AS response surface can indeed be used as a low-fidelity purely data-driven model in the process of design of a multi-fidelity model, along with more standard models based on different physical or numerical approximations of the phenomenon under study. It must be said that the RANS outputs are poorly correlated with respect to the DDES as can be seen from Figure 14: in fact the converged GPR built upon the RANS training dataset have a mean R^2 score below 0 on the DDES test set. Nonetheless, the multi-fidelity model DDES-RANS achieves an accuracy higher than the single-fidelity DDES model.

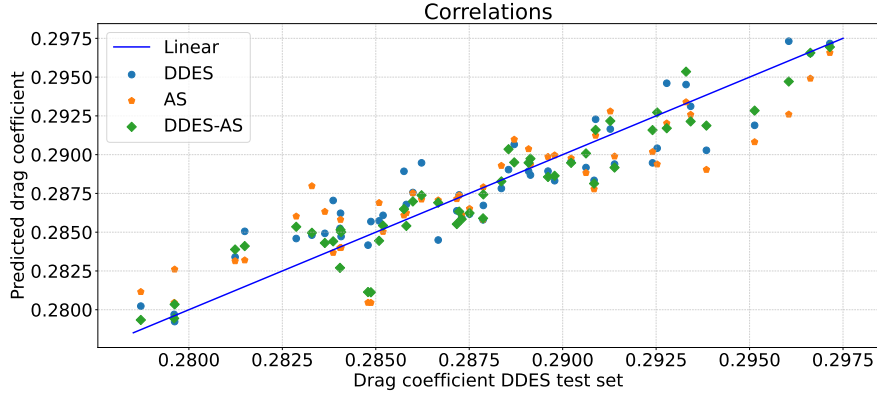


Figure 13: Comparison of the correlations between the predictions of the DDES model with the test DDES outputs and the correlations between the DDES-AS MF model with the test DDES outputs.

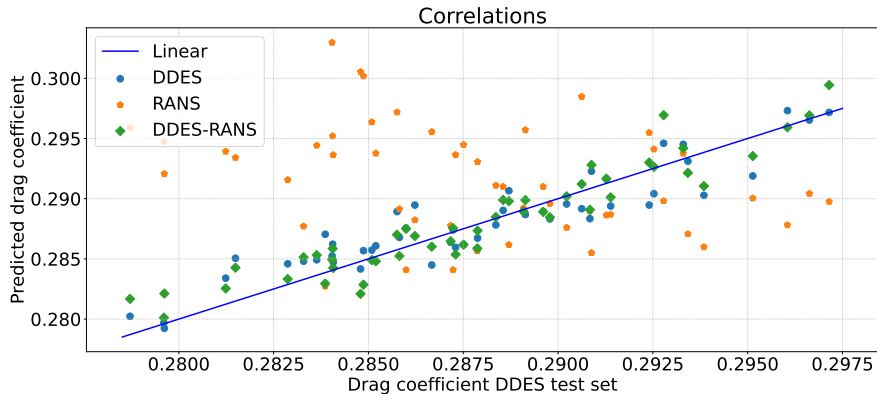


Figure 14: Comparison of the correlations between the predictions of the DDES model with the test DDES outputs, the correlations between the RANS model with the test DDES outputs, and the correlations between the DDES-RANS model with the test DDES outputs.

6 Conclusions and future perspectives

The approximation of high-dimensional scalar quantities of interest is a challenging problem in the context of data scarcity, which is typical in engineering applications. We addressed this problem by proposing a nonlinear multi-fidelity method which does not necessitate the simulation of simplified models, but instead constructs a low-fidelity surrogate introducing a low-intrinsic dimensionality bias through active subspaces or nonlinear level-set learning methods. Our approach is data-efficient since it extracts new information from the high-fidelity simulations. We construct different Gaussian processes using the autoregressive scheme called NARGP. The proposed multi-fidelity approach results in better approximation accuracy over the entire parameter space as demonstrated with two benchmark problems and an automotive application.

NARGP-AS was able to achieve better performance with respect to the single-fidelity GP over the high-fidelity data, resulting in a relative gain on the R^2 score around 3–5% for the piston model, and around 3–4% for the Ebola model, depending on the number of samples used. NARGP-NLL was used for the Jetta-6 test case, reaching an accuracy gain around 2% with respect to the low-fidelity model, and around 4% with respect to the high-fidelity model. We also presented a comparison switching the two fidelities. Finally for the Jetta-12 test case we obtained a relative gain on the R^2 score around 3%.

Future research lines should investigate the use of different active subspaces-based methods, such as kernel AS [42], or local AS [43], which exploit kernel-based and localization techniques, respectively. This multi-fidelity framework has also the potential to be integrated with other

reduced order modeling techniques [46, 7, 47] to further increase the accuracy in the resolution of parametric problems, especially for high-dimensional surrogate-based optimization [51].

Mandatory for real applications is a model management strategy providing theoretical guarantees and establishing accuracy and/or convergence of outer-loop applications. Some attempts towards multi-source Bayesian optimization/Experimental design are being studied. Moreover increasing the number of fidelities in the multi-fidelity model is a possible direction of investigation, especially when the phenomenon of interest allows many cheap low-fidelity approximations.

Acknowledgements

This work was partially supported by the European Commission H2020 ARIA (Accurate ROMs for Industrial Applications) project, by an industrial Ph.D. grant sponsored by Fincantieri S.p.A. (IRONTH Project), by MIUR (Italian ministry for university and research) through FARE-X-AROMA-CFD project, by the European Commission H2020 UPSCALE project (Upscaling product development simulation capabilities exploiting artificial intelligence for electric vehicles, 824306), and partially funded by European Union Funding for Research and Innovation — Horizon 2020 Program — in the framework of European Research Council Executive Agency: H2020 ERC CoG 2015 AROMA-CFD project 681447 “Advanced Reduced Order Methods with Applications in Computational Fluid Dynamics” P.I. Professor Gianluigi Rozza.

References

- [1] Upscale (upscaling product development simulation capabilities exploiting artificial intelligence for electric vehicles). <https://www.upscaleproject.eu/>, 2021. [Online; accessed 2023-01-04].
- [2] E. N. Ben-Ari and D. M. Steinberg. Modeling data from computer experiments: an empirical comparison of kriging with MARS and projection pursuit regression. *Quality Engineering*, 19(4):327–338, 2007. doi:10.1080/08982110701580930.
- [3] L. Bonfiglio, P. Perdikaris, S. Brizzolara, and G. Karniadakis. Multi-fidelity optimization of super-cavitating hydrofoils. *Computer Methods in Applied Mechanics and Engineering*, 332:63–85, 2018. doi:10.1016/j.cma.2017.12.009.
- [4] L. Bonfiglio, P. Perdikaris, G. Vernengo, J. S. de Medeiros, and G. Karniadakis. Improving SWATH Seakeeping Performance using Multi-Fidelity Gaussian Process and Bayesian Optimization. *Journal of Ship Research*, 62(4):223–240, 2018. doi:10.5957/JOSR.11170069.
- [5] R. A. Bridges, A. D. Gruber, C. R. Felder, M. Verma, and C. Hoff. Active Manifolds: A non-linear analogue to Active Subspaces. In *Proceedings of the 36th International Conference on Machine Learning, ICML 2019*, pages 764–772, Long Beach, California, USA, 9–15 June 2019.
- [6] B. Chang, L. Meng, E. Haber, L. Ruthotto, D. Begert, and E. Holtham. Reversible architectures for arbitrarily deep residual neural networks. In *Proceedings of the AAAI Conference on Artificial Intelligence*, volume 32, 2018.
- [7] F. Chinesta, A. Huerta, G. Rozza, and K. Willcox. Model reduction methods. In E. Stein, R. de Borst, and T. J. R. Hughes, editors, *Encyclopedia of Computational Mechanics, Second Edition*, pages 1–36. John Wiley & Sons, Ltd., 2017.
- [8] P. G. Constantine. *Active subspaces: Emerging ideas for dimension reduction in parameter studies*, volume 2 of *SIAM Spotlights*. SIAM, -, 2015. doi:10.1137/1.9781611973860.
- [9] P. G. Constantine and P. Diaz. Global sensitivity metrics from active subspaces. *Reliability Engineering & System Safety*, 162:1–13, 2017. doi:10.1016/j.ress.2017.01.013.
- [10] P. G. Constantine, C. Kent, and T. Bui-Thanh. Accelerating Markov Chain Monte Carlo with Active Subspaces. *SIAM Journal on Scientific Computing*, 38(5):A2779–A2805, 2016. doi:10.1137/15M1042127.

- [11] A. Damianou and N. Lawrence. Deep Gaussian processes. In *Artificial Intelligence and Statistics*, pages 207–215, 2013.
- [12] N. Demo, M. Tezzele, A. Mola, and G. Rozza. Hull Shape Design Optimization with Parameter Space and Model Reductions, and Self-Learning Mesh Morphing. *Journal of Marine Science and Engineering*, 9(2):185, 2021. doi:10.3390/jmse9020185.
- [13] N. Demo, M. Tezzele, and G. Rozza. A non-intrusive approach for reconstruction of POD modal coefficients through active subspaces. *Comptes Rendus Mécanique de l’Académie des Sciences*, 347(11):873–881, November 2019. doi:10.1016/j.crme.2019.11.012.
- [14] N. Demo, M. Tezzele, and G. Rozza. A Supervised Learning Approach Involving Active Subspaces for an Efficient Genetic Algorithm in High-Dimensional Optimization Problems. *SIAM Journal on Scientific Computing*, 43(3):B831–B853, 2021. doi:10.1137/20M1345219.
- [15] P. Diaz, P. Constantine, K. Kalmbach, E. Jones, and S. Pankavich. A modified SEIR model for the spread of Ebola in Western Africa and metrics for resource allocation. *Applied Mathematics and Computation*, 324:141–155, 2018. doi:10.1016/j.amc.2017.11.039.
- [16] A. I. Forrester, A. Sóbester, and A. J. Keane. Multi-fidelity optimization via surrogate modelling. *Proceedings of the Royal Society A: Mathematical, Physical and Engineering Sciences*, 463(2088):3251–3269, 2007. doi:10.1098/rspa.2007.1900.
- [17] S. F. Ghoreishi, S. Friedman, and D. L. Allaire. Adaptive Dimensionality Reduction for Fast Sequential Optimization With Gaussian Processes. *Journal of Mechanical Design*, 141(7):071404, 2019. doi:10.1115/1.4043202.
- [18] GPy. GPy: A Gaussian process framework in Python. <http://github.com/SheffieldML/GPy>, since 2012.
- [19] E. Haber and L. Ruthotto. Stable architectures for deep neural networks. *Inverse problems*, 34(1):014004, 2017. doi:10.1088/1361-6420/aa9a90.
- [20] A. Holiday, M. Kooshkbaghi, J. M. Bello-Rivas, C. W. Gear, A. Zagaris, and I. G. Kevrekidis. Manifold learning for parameter reduction. *Journal of computational physics*, 392:419–431, 2019. doi:10.1016/j.jcp.2019.04.015.
- [21] M. Kanagawa, P. Hennig, D. Sejdinovic, and B. K. Sriperumbudur. Gaussian processes and kernel methods: A review on connections and equivalences. *arXiv preprint arXiv:1807.02582*, 2018.
- [22] M. C. Kennedy and A. O’Hagan. Predicting the output from a complex computer code when fast approximations are available. *Biometrika*, 87(1):1–13, 2000.
- [23] D. P. Kingma and J. Ba. Adam: A method for stochastic optimization. In *International Conference on Learning Representations (ICLR)*, 2015.
- [24] B. Kramer, A. N. Marques, B. Peherstorfer, U. Villa, and K. Willcox. Multifidelity probability estimation via fusion of estimators. *Journal of Computational Physics*, 392:385–402, 2019. doi:10.1016/j.jcp.2019.04.071.
- [25] R. R. Lam, O. Zahm, Y. M. Marzouk, and K. E. Willcox. Multifidelity Dimension Reduction via Active Subspaces. *SIAM Journal on Scientific Computing*, 42(2):A929–A956, 2020. doi:10.1137/18M1214123.
- [26] M. Lázaro-Gredilla, J. Quiñonero-Candela, C. E. Rasmussen, and A. R. Figueiras-Vidal. Sparse spectrum Gaussian process regression. *The Journal of Machine Learning Research*, 11:1865–1881, 2010.
- [27] M. Lázaro-Gredilla and M. K. Titsias. Variational Heteroscedastic Gaussian Process regression. In *Proceedings of the 28th International Conference on International Conference on Machine Learning, ICML’11*, pages 841–848, Madison, WI, USA, 2011. Omnipress.

- [28] L. Le Gratiet and J. Garnier. Recursive co-kriging model for design of computer experiments with multiple levels of fidelity. *International Journal for Uncertainty Quantification*, 4(5):365–386, 2014. doi:10.1615/Int.J.UncertaintyQuantification.2014006914.
- [29] H. Liu, Y.-S. Ong, X. Shen, and J. Cai. When Gaussian process meets big data: A review of scalable GPs. *IEEE Transactions on Neural Networks and Learning Systems*, 2020.
- [30] T. W. Lukaczyk, P. Constantine, F. Palacios, and J. J. Alonso. Active subspaces for shape optimization. In *10th AIAA multidisciplinary design optimization conference*, page 1171, 2014. doi:10.2514/6.2014-1171.
- [31] X. Meng and G. E. Karniadakis. A composite neural network that learns from multi-fidelity data: Application to function approximation and inverse PDE problems. *Journal of Computational Physics*, 401:109020, 2020. doi:10.1016/j.jcp.2019.109020.
- [32] M. Mrosek, C. Othmer, and R. Radespiel. Reduced-order modeling of vehicle aerodynamics via proper orthogonal decomposition. *SAE International Journal of Passenger Cars — Mechanical Systems*, 12:225–236, 10 2019. doi:10.4271/06-12-03-0016.
- [33] H. Nguyen, J. Wittmer, and T. Bui-Thanh. DIAS: A Data-Informed Active Subspace Regularization Framework for Inverse Problems. *Computation*, 10(3):38, 2022.
- [34] T. O’Leary-Roseberry, U. Villa, P. Chen, and O. Ghattas. Derivative-informed projected neural networks for high-dimensional parametric maps governed by pdes. *Computer Methods in Applied Mechanics and Engineering*, 388:114199, 2022. doi:10.1016/j.cma.2021.114199.
- [35] C. Othmer, T. W. Lukaczyk, P. Constantine, and J. J. Alonso. On active subspaces in car aerodynamics. In *17th AIAA/ISSMO Multidisciplinary Analysis and Optimization Conference*, page 4294, 2016. doi:10.2514/6.2016-4294.
- [36] A. Paleyes, M. Pullin, M. Mahsereci, N. Lawrence, and J. González. Emulation of physical processes with Emukit. In *Second Workshop on Machine Learning and the Physical Sciences, NeurIPS*, 2019.
- [37] A. Paszke, S. Gross, F. Massa, A. Lerer, J. Bradbury, G. Chanan, T. Killeen, Z. Lin, N. Gimelshein, L. Antiga, A. Desmaison, A. Kopf, E. Yang, Z. DeVito, M. Raison, A. Tejani, S. Chilamkurthy, B. Steiner, L. Fang, J. Bai, and S. Chintala. Pytorch: An imperative style, high-performance deep learning library. In H. Wallach, H. Larochelle, A. Beygelzimer, F. d’Alché-Buc, E. Fox, and R. Garnett, editors, *Advances in Neural Information Processing Systems 32*, pages 8024–8035. Curran Associates, Inc., -, 2019.
- [38] P. Perdikaris, M. Raissi, A. Damianou, N. D. Lawrence, and G. E. Karniadakis. Nonlinear information fusion algorithms for data-efficient multi-fidelity modelling. *Proceedings of the Royal Society A*, 473(2198):20160751, 2017. doi:10.1098/rspa.2016.0751.
- [39] D. Pozharskiy, N. J. Wichrowski, A. B. Duncan, G. A. Pavliotis, and I. G. Kevrekidis. Manifold learning for accelerating coarse-grained optimization. *Journal of Computational Dynamics*, 7(2):511–536, 2020. doi:10.3934/jcd.2020021.
- [40] M. Raissi, P. Perdikaris, and G. E. Karniadakis. Inferring solutions of differential equations using noisy multi-fidelity data. *Journal of Computational Physics*, 335:736–746, 2017. doi:10.1016/j.jcp.2017.01.060.
- [41] M. Raissi, P. Perdikaris, and G. E. Karniadakis. Physics-informed neural networks: A deep learning framework for solving forward and inverse problems involving nonlinear partial differential equations. *Journal of Computational Physics*, 378:686–707, 2019. doi:10.1016/j.jcp.2018.10.045.
- [42] F. Romor, M. Tezzele, A. Lario, and G. Rozza. Kernel-based active subspaces with application to computational fluid dynamics parametric problems using discontinuous Galerkin method. *International Journal for Numerical Methods in Engineering*, 123(23):6000–6027, 2022. doi:10.1002/nme.7099.

- [43] F. Romor, M. Tezzele, and G. Rozza. A local approach to parameter space reduction for regression and classification tasks. *arXiv preprint arXiv:2107.10867*, 2021.
- [44] F. Romor, M. Tezzele, and G. Rozza. ATHENA: Advanced Techniques for High dimensional parameter spaces to Enhance Numerical Analysis. *Software Impacts*, page 100133, 2021. doi:10.1016/j.simpa.2021.100133.
- [45] F. Romor, M. Tezzele, and G. Rozza. Multi-fidelity data fusion for the approximation of scalar functions with low intrinsic dimensionality through active subspaces. In *Proceedings in Applied Mathematics & Mechanics*, volume 20. Wiley Online Library, 2021. doi:10.1002/pamm.202000349.
- [46] G. Rozza, M. Hess, G. Stabile, M. Tezzele, and F. Ballarin. Basic Ideas and Tools for Projection-Based Model Reduction of Parametric Partial Differential Equations. In P. Benner, S. Grivet-Talocia, A. Quarteroni, G. Rozza, W. H. A. Schilders, and L. M. Silveira, editors, *Model Order Reduction*, volume 2, chapter 1, pages 1–47. De Gruyter, Berlin, Boston, 2020. doi:10.1515/9783110671490-001.
- [47] G. Rozza, G. Stabile, and F. Ballarin. *Advanced Reduced Order Methods and Applications in Computational Fluid Dynamics*. SIAM, 2022. doi:10.1137/1.9781611977257.
- [48] E. Snelson, Z. Ghahramani, and C. E. Rasmussen. Warped Gaussian processes. In S. Thrun, L. Saul, and B. Schölkopf, editors, *Advances in Neural Information Processing Systems*, volume 16, pages 337–344, -, 2004. MIT Press.
- [49] M. Tezzele, F. Ballarin, and G. Rozza. Combined parameter and model reduction of cardiovascular problems by means of active subspaces and POD-Galerkin methods. In D. Boffi, L. F. Pavarino, G. Rozza, S. Scacchi, and C. Vergara, editors, *Mathematical and Numerical Modeling of the Cardiovascular System and Applications*, volume 16 of *SEMA-SIMAI Series*, pages 185–207. Springer International Publishing, -, 2018. doi:10.1007/978-3-319-96649-6_8.
- [50] M. Tezzele, N. Demo, G. Stabile, A. Mola, and G. Rozza. Enhancing CFD predictions in shape design problems by model and parameter space reduction. *Advanced Modeling and Simulation in Engineering Sciences*, 7(40), 2020. doi:10.1186/s40323-020-00177-y.
- [51] M. Tezzele, L. Fabris, M. Sidari, M. Sicchiero, and G. Rozza. A multi-fidelity approach coupling parameter space reduction and non-intrusive POD with application to structural optimization of passenger ship hulls. *International Journal for Numerical Methods in Engineering*, 124(5):1193–1210, 2023. doi:10.1002/nme.7159.
- [52] M. Tezzele, F. Salmoiraghi, A. Mola, and G. Rozza. Dimension reduction in heterogeneous parametric spaces with application to naval engineering shape design problems. *Advanced Modeling and Simulation in Engineering Sciences*, 5(1):25, Sep 2018. doi:10.1186/s40323-018-0118-3.
- [53] H. G. Weller, G. Tabor, H. Jasak, and C. Fureby. A tensorial approach to computational continuum mechanics using object-oriented techniques. *Computers in physics*, 12(6):620–631, 1998. doi:10.1063/1.168744.
- [54] C. K. Williams and C. E. Rasmussen. *Gaussian Processes for Machine Learning*. Adaptive Computation and Machine Learning series. MIT press Cambridge, MA, -, 2006.
- [55] N. Wycoff, M. Binois, and S. M. Wild. Sequential Learning of Active Subspaces. *Journal of Computational and Graphical Statistics*, pages 1–14, 2021. doi:10.1080/10618600.2021.1874962.
- [56] O. Zahm, P. G. Constantine, C. Prieur, and Y. M. Marzouk. Gradient-based dimension reduction of multivariate vector-valued functions. *SIAM Journal on Scientific Computing*, 42(1):A534–A558, 2020. doi:10.1137/18M1221837.
- [57] G. Zhang, J. Zhang, and J. Hinkle. Learning nonlinear level sets for dimensionality reduction in function approximation. In *Advances in Neural Information Processing Systems*, pages 13199–13208, 2019.